Evanescent microwave probes and microscopy

A. García-Valenzuela
Laboratorio de Óptica Aplicada, Centro de Instrumentos, Universidad Nacional Autónoma de México
Apartado postal 70-186, 04510 México, D.F., Mexico.
e-mail: garciaa@aleph.cinstrum.unam.mx

M. Tabib-Azar
Electrical Engineering and Computer Science Department, Case Western Reserve University
10900 Euclid Av., Cleveland OH 44106, USA

Recibido el 20 de agosto de 1999; aceptado el 9 de septiembre de 1999

Evanescent microwave probes have gained considerable attention recently. These probes can obtain measurements of the microwave properties of materials with a very high spatial resolution. By scanning the probe across the area of interest images of the topography, subsurface features, or microwave parameters can be generated for a large variety of materials. In this article, we review the development and present state of evanescent microwave probes and their use in microscopy. We formulate a simple model of an evanescent probe and discuss its basic principles and potential as a nondestructive testing tool for a variety of applications. We address important issues regarding the fundamental differences with other electromagnetic probes, the spatial resolution, and the sensitivity to changes in the sample's parameters. We summarize recent work on applications of these probes with different materials. The present paper gives motivation and the basic tools for further research into applications and fundamental issues of these probes.

Keywords: Microwaves; evanescent fields; microscopy; characterization of materials

Las sondas de microondas evanescentes han llamado considerablemente la atención recientemente. Estos instrumentos pueden obtener mediciones de las características de los materiales en el rango de las microondas con una alta resolución espacial. Haciendo un barrido de la sonda a través del área de interés se pueden generar imágenes de la topografía, defectos sub-superficiales y de las propiedades del material a la frecuencia de operación para una gran variedad de materiales. En este artículo, presentamos una revisión del desarrollo y el estado actual de este tipo de instrumentos y su uso en microscopía. Formulamos un modelo sencillo de una sonda evanescente y discutimos su principio básico y su potencial como herramienta de pruebas no destructivas en diferentes aplicaciones. Consideramos aspectos importantes referentes a las diferencias con otro tipo de sondas electromagnéticas, la resolución espacial, y la sensibilidad al cambio en las propiedades del material de prueba. Resumimos el trabajo reciente en cuanto a las aplicaciones de estas sondas con diferentes materiales. Este artículo pretende motivar y dar las herramientas básicas para continuar la investigación en los aspectos fundamentales y las aplicaciones de estos instrumentos.

Descriptores: Microondas; campos evanescentes; microscopía; caracterización de materiales

PACS: 07.57.-c; 07.79.-v; 07.07

1. Introduction

In the last two decades, there has been an increasing interest on the development of probe microscopy techniques. After the introduction of the scanning tunneling microscopy (STM) in 1982 [1, 2], many other important techniques based on the local interaction of a sharp tip and sample were proposed and some are still under investigation. These techniques include atomic force [3, 4], magnetic force [5], thermal [6], ion conductance [7], near-field optical [8], and capacitance [9] scanning microscopy. In particular, atomic force microcopy has become very popular due to its potential to image with atomic resolution very different kinds of surfaces. Other probe techniques which have drawn many researchers attention in later years is the scanning near-field optical microscope (NSOM) [10–15] and scanning capacitance microscopy (SCM) [16–19]. Evanescent microwave probes (EMP) have also been considered recently and at the time, the potential of these EMP appears to be very promising with a larger spectrum of applications. In fact, EMP may be found to be related to NSOM and to SCM.

The limit resolution of near-field probes is one of the main issues. In conventional optical microscopes, the spatial resolution limit is in the order of the wavelength used. Specifically, the smallest resolvable spacing between two point sources is $\lambda/2\sin\alpha$, where α is the collection angle that the aperture subtends. This limit is known as the Abbe barrier, or the diffraction-limited resolution, and is due to diffraction phenomena inherent to the wave phenomena. Thus is "unbreakable". However, this limit only applies to the conventional way of imaging using lenses. It does not apply to scanning near-field microscopes, since diffraction, in the strict sense of the term, is not involved in the probe-sample interaction. Nevertheless, the wavelength of radiation does play a role in some cases, and a good figure of merit of a microscope involving some kind of wave phenomena, is the spatial resolution in terms of the wavelength. However in some cases such figure of merit is not useful; *e.g.*, in capacitance and electrostatic techniques the wavelength is considered infinite.

The limit to the spatial resolution in a near field microscope has to do more with the possibility to confine power flux through a small area (the tip). Wavelength may or may not play a dominant role in such limit. Resolution, spatial or with respect to changes on the sample properties, depends on the minimum detectable change in the coupling between sample and probe.

2. Historic outline

Synge is credited for suggesting for the first time near-field microscopy [20] in 1928. Electromagnetic evanescent fields were considered quantitatively by Bethe in calculating the coupling efficiency of microwave waveguides through a small aperture much smaller than the wavelength in 1944 [21]. Baez discussed sub-wavelength resolution and gave a proof of principle experiment using an audio oscillator in 1956 [22]. The first experimental demonstration of imaging with evanescent fields at microwave frequencies was carried out by Soohoo in 1962 [23], and in 1972 Ash and Nicholls demonstrated that microwave evanescent fields could be used the image features on the order of $\lambda/100$ [24].

With the introduction of the scanning tunneling microscope (STM), the technology to manipulate a small tip with sub-nanometer precision evolved rapidly (being now commercially available). The present technology is based on piezoelectric micropositioners. Contrary to what one may expect, the technology is very simple (although costs can not be overlooked yet). An accessible description of it is found in the book by C. Julian Chen [25]. As indicated above, STM and the scanning technology on an atomic-level that came with it, triggered many to search for new probe techniques for microscopy based on different physical phenomena (atomic force, magnetic, optical, ionic transport, etc.). In particular atomic force microscopy (AFM) soon followed STM [3, 4, 25], being both very popular today. Atomic force microscopy turned out to be more versatile, since there is no need of a conducting sample, and is perhaps more widely used today. Electromagnetic probes at optical frequencies followed rapidly. Pohl and coworkers reported an optical stethoscope with a spatial resolution appreciably less than the wavelength in 1984 [8]. Their work started few years before, and a patent application predates the article [14]. In a second publication in 1986, they called their instrument a near-field optical scanning microscope (NSOM) [10]. Their microscope consisted of a sharp quartz-tip covered with an aluminum film with a small aperture at the apex. Independently, Lewis and coworkers reported results of sub-wavelength resolution in 1983 [11], and later showed evanescent field images of a gratin in 1986 [12]. Evanescent field microwave probes with sub-wavelength resolution using a transmission line were considered in 1987 by Gutmann *et al.* for planar structure diagnosis [26], but no further works with MW followed short after. Since the mid 80's NSOM has caught the attention of numerous experimentalists and theoreticians, being today a very active area of research [15]. For a detailed overview of different types of NSOM which have been explored, basic principles and instrumentation the reader is referred to the book in Ref. 13.

Scanning capacitance microscopy (SCM) also followed the introduction of the STM [9, 16]. In 1989 Williams *et al.* reported a SCM on a 25 nm scale [17]. SCM consists of measuring the capacitance between a sharp tip and the sample. High sensitivity to capacitance variations (resolution in the order of 1×10^{-19} F) is achieved using a resonant circuit [17–19]. The general character of the images obtained with a SCM is similar to that of a STM but with less spatial resolution. However, in SCM the sample may be covered by a thin dielectric layer (many times this layer is formed naturally after exposure to air). This is a virtue of SCM in that imaging of a conductor through a dielectric layer is possible.

Combinations of probe microscopy techniques were also introduced. In particular SCM and AFM were combined in 1991 by Barret and Quate [18]. They placed a conducting tip on an AFM cantilever. The tip was pressed to a thin dielectric layer formed on top of the conducting sample. Measuring deflections of the cantilever gave in addition topographical information of the surface. The main purpose of their instrument was to measure the charge storage in a nitride-oxide-silicon system.

Evanescent microwave probes were again considered until 1993 by Tabib-Azar and coworkers in [27]. A microstrip quarter wavelength resonator in conjunction with a small probe was used to map microwave conductivity variations in metallic lines on circuit boards and of a silicon wafer. The possibility of using electric dipole probes as well as magnetic dipole probes in high resolution imaging was demonstrated. Imaging of subsurface defects was shown to be feasible by detecting holes in a printed circuit board that were covered by solder and were not visible. Spatial resolution on the order of $\lambda/1000$ was achieved. Since then, other groups have started working on EMP.

Xiang and coworkers reported in 1996 a scanning tip near-field microscope at radio/microwave frequencies. The microscope consisted of a $\lambda/4$ coaxial resonator with a tapered center conductor, a sharpened tip which is connected to the center conductor and protrudes from an aperture on a shielding plate connected to the outer conductor. In their first publication a spatial resolution of 5 μm was reported [28]. In a subsequent publication from the same laboratory, Gao et al reported an improved instrument with a sharper tip achieving a 100 nm spatial resolution while imaging dielectric samples (corresponding to $\lambda/10^6$). The tip was in soft contact with the sample. A resolution on the difference of the dielectric constant that could be detectable of $\delta\varepsilon/\varepsilon \approx 6 \times 10^{-4}$ was reported [29].

Also in 1996 Vlahacos *et al.* [30] reported a simple near-field scanning microwave microscope with a spatial resolution of about 100 μm, and operating in the 8–12 GHz range, corresponding to $\lambda/360$ at 12 GHz. They used a 2 m-long resonant coaxial transmission-line connected to an open-ended

coaxial probe. No tapering of the inner conductor nor shielding plate was used. In a second publication by the same group [31], Steinhauer et al monitored the frequency shift of the resonance as the open end of the transmission line was scanned closely to the sample, using a frequency-following circuit. A sensitivity to frequency shifts of 2 parts in 10^6 during a 30 ms sampling time was achieved. They used their EMP to map surface resistance of metallic samples. They estimated a resolution in surface resistance of $\Delta R_X/R_X = 0.05$ for $R_X = 100\omega/\Box$.

The applicability and versatility of EMP for their use with very different kind of material is illustrated by a series of recent papers from the group of M. Tabib-Azar [32–39]. Microstrip or strip line resonators were used in the latter works, illustrating their use with metal, semiconductors and insulators, and with biological and relevant medical samples.

Quantitative interpretations of the images require accurate models of the tip and tip-sample interaction. Relatively few works have been dedicated so far to the theoretical models. Two recent papers give the foundations for such work [40, 41]. In Ref. 40 Gao and Xiang proposed a quantitative theoretical model for imaging dielectric samples. They modeled the tip as a conducting sphere. They considered in particular the case of imaging dielectrics (with real and complex dielectric constant). They allow a soft contact of the tip and sample, which enhance spatial resolution. Comparison with experiment showed to be in good agreement. They showed that the spatial resolution can be two orders of magnitude less than the radius of the sphere (tip) when $\varepsilon > 50\,\varepsilon_0$. Their estimations indicate that nanometer spatial resolution is achievable (100 nm spatial resolution has been achieved already for $\varepsilon > 20\,\varepsilon_0$ [19]). Such a resolution would be comparable with that of NSOMs, but using a wavelength 10^5 times larger. The resolutions to changes in the dielectric constant is estimated in the order of $\delta\varepsilon/\varepsilon \approx 10^{-5}$ for such a probe. Tabib Azar *et al.*, presents a detailed analysis of the sensitivity of the resonator to perturbations due to tip-sample interaction [41]. Simple formulas for the resolution, spatial and on changes in conductivity and dielectric constant, are given. The possibility of 100 nm spatial resolutions using the microstrip resonator are predicted. Resolutions of $\delta\sigma/\sigma \approx 10^{-2}$ in metals, $\delta\sigma/\sigma \approx 10^{-4}$ in semiconductors, and of $\delta\varepsilon/\varepsilon \approx 10^{-3}$ in dielectrics is predicted for such a probe. An approach to enhance the spatial resolution by deconvolving the EMP image with the experimentally measured spatial impulse response is investigated in Ref 42.

Finally, new analytical tools are being investigated by García-Valenzuela *et al.* to calculate the capacitance between electrodes with arbitrarily rough surfaces [43, 44]. The approach is based on perturbative solutions to the boundary integral equation. Extensions of the results to model the coupling capacitance between a tip and a rough surface are still to be done. Nevertheless, to date it appears that this is the most attractive approach to obtain analytical models for interpretation of very high resolution two-dimensional topographical images.

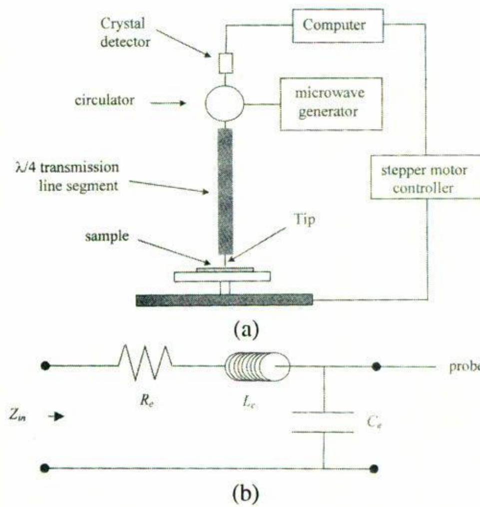

FIGURE 1. a) Schematic layout of an EMP. b) Equivalent circuit of the $\lambda/4$ resonator near resonance.

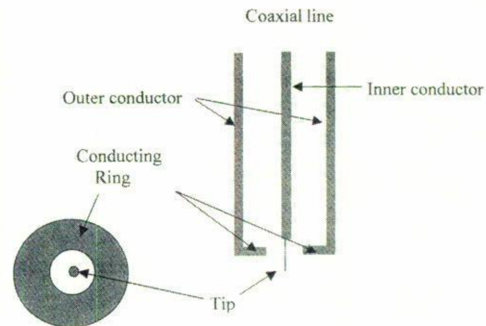

FIGURE 2. Side and bottom views of a possible tip geometry.

3. Basic model of a EMP

The EMP consists of a short open-ended transmission-line which couples to the sample through a sharp tip (see Figs. 1 and 2). The effective length, ℓ, of the transmission line should be close to $\lambda/4$. It is not difficult to show that a quarter-wavelength transmission line is equivalent to a series resonant circuit [45]. The equivalent circuit analysis is used by several authors in previous works to model the probe sensitivity [30, 40, 41]. In what follows we summarize the electrical aspects of the probe.The magnitude of the reflection coefficient of a voltage wave impinging onto the resonator, $|S_{11}|$, is measured, using for example a circulator and a square law detector [41], as illustrated in Fig. 1a. The simplest method to image a sample with a EMP is to keep a constant frequency f_x, and tip-sample distance d_1, and measure the resonator's reflection coefficient, $|S_{11}|$ as the probe is scanned across the sample's surface. Other possibilities are to keep $|S_{11}|$ and d_1 constant using a feedback circuitry and measuring f_x, and keeping $|S_{11}|$ and f_x constant and measuring d_1. We will consider only the first case, since it is the simplest. Different kinds of transmission lines are possible.

3.1. Analysis of the resonator

The reflection coefficient of the resonator is given by

$$S_{11} = \frac{Z_{in} - Z_{0f}}{Z_{in} + Z_{0f}}, \quad (1)$$

where Z_{in} is the input impedance of the resonator and Z_{0f} is the characteristic impedance of the feed line. Using stantard transmission line theory, Z_{in} is given by

$$Z_{in} = Z_0 \frac{1 + \Gamma \exp(-2\gamma\ell)}{1 - \Gamma \exp(-2\gamma\ell)}, \quad (2)$$

where $Z_0 = \sqrt{L/C}$ is the characteristic impedance of the resonator line, Γ is the reflection coefficient at the tip-end of the resonator, and $\gamma = \alpha + j\beta$, where j is the imaginary unit. For a low loss line $\alpha = \frac{1}{2}R\sqrt{C/L}$ and $\beta = \omega\sqrt{CL}$, where ω is the radial frequency, R, C, and L, are the resistance, capacitance, and inductance per unit length of the resonator's line, respectively.

If there is no tip-sample coupling, the reflection coefficient at the end of the probe is $\Gamma = 1$ (assuming the open-circuited end). In this case, resonance ($\omega = \omega_0$), is defined by $\exp(2j\beta\ell) = -1$, *i.e.*, $\beta\ell = \pi/2$. Thus, $\omega_0 = \pi/(2\ell\sqrt{LC})$. If α is zero (a loss-less line), so is the input impedance, and the admittance is infinte. Assuming very low losses ($2\alpha\ell \ll 1$), and a frequency ω close to resonance: $\beta(\omega_0 + \Delta\omega)\sqrt{LC} = \pi/2\ell + \Delta\omega\sqrt{LC}$; with $\Delta\omega\sqrt{LC} \ll 1/\lambda$, we get from (2), $Z_{in} = Z_0(\alpha\ell + j\Delta\omega L\ell)$, where we kept terms of first order in smallness. The resistance and inductance of the resonator are defined as $R_0 = \frac{1}{2}R\ell$ and $L_0 = \frac{1}{2}L\ell$, thus we may write

$$Z_{in} = R_0 + 2j\Delta\omega L_0. \quad (3)$$

The factors $\frac{1}{2}$ in the relations $R_0 = \frac{1}{2}R\ell$ and $L_0 = \frac{1}{2}L\ell$ are due to sinusoidal dependence of the voltage and current across the resonator. Note that at resonance the impedance is real and smallest, the admittance is largest.

The circuit equivalent of the transmission line resonator of an EMP near resonance is shown in Fig. 1b. The resonance frequency of the equivalent circuit is $1/\sqrt{L_e C_e}$, which is equal to ω_0 given above, provided $L_e = L_o = \frac{1}{2}\ell L$, and $C_e = 8\ell C/\pi^2$, where C is the capacitance per unit length of the resonator. The Q-factor is defined considering the admittance $Y_{in} = 1/Z_{in}$, which is maximum at resonance. It is defined as the fractional bandwidth between the points where $|Y_{in}|$ is 0.707 of its maximum value. From (3) we may find $Q = L_0\omega_0/R_0$, and we may write

$$Z_{in} = R_0 \left(1 + 2jQ\frac{\Delta\omega}{\omega_0}\right). \quad (4)$$

If the probe approaches the sample, coupling to the sample will deviate the reflection coefficient Γ form unity. An EMP should operate under weak coupling to the sample. Thus we may approximate

$$\Gamma = \frac{Z_l - Z_0}{Z_l + Z_0} \approx 1 - \frac{2Z_0}{Z_l}, \quad (5)$$

where $Z_l (\gg Z_0)$ is the load impedance. For clarity in the following equations let us define the complex perturbing term, $g(\omega) = g_r(\omega) + jg_i(\omega) = -2Z_0/Z_l$. Assuming very low losses in the resonator, and a frequency ω close to the resonance frequency of the unperturbed resonator ω_0, we get using (2),

$$Z_{in} = R_0 + 2j\Delta\omega L_0 - \tfrac{1}{2}Z_0 g(\omega), \quad (6)$$

where we kept terms of first order in smallness only. The new resonance frequency (ω_0') is where the imaginary component in (6) is zero. Using $\Delta\omega = \omega - \omega_0$, we get

$$2(\omega_0' - \omega_0)L_0 - \tfrac{1}{2}Z_0 g_i(\omega_0') = 0, \quad (7)$$

from where we solve for ω_0'. The inductance and resistance of the perturbed resonator is found from rewriting Z_{in} in terms of $\Delta\omega' = \omega - \omega_0'$. Using $g_i(\omega) \cong g_i(\omega_0') + (dg_i/d\omega)|_{\omega_0'}$ $\Delta\omega'$, $2jL_0\Delta\omega = 2jL_0(\Delta\omega' + \omega_0' - \omega_0)$ we get from above,

$$Z_{in} = R_0 - \frac{1}{2}Z_0 g_r(\omega) - \left[2jL_0 - \frac{1}{2}jZ_0\left(\frac{dg_i}{d\omega}\right)\bigg|_{\omega_0'}\right]\Delta\omega', \quad (8)$$

which we may rewrite as

$$Z_{in} = R_0' + 2jL_0'\Delta\omega' = R_0'\left(1 + 2jQ'\frac{\Delta\omega'}{\omega_0'}\right), \quad (9a)$$

where

$$R_0' = R_0 - \tfrac{1}{2}Z_0\, g_r(\omega),$$
$$L_0' = L_0 - \frac{1}{4}Z_0\left(\frac{dg_i}{d\omega}\right)\bigg|_{\omega_0'}, \quad (9b)$$

and

$$Q' = \frac{L_0'\omega_0'}{R_0'}$$

3.2. Probe-sample coupling

Different tip geometries have been used, depending on the kind of transmission line used for the resonator (microstrip, coaxial, etc.). In essence, all tips will work under the same basic principles. From a conceptual point of view it is convenient to consider the one depicted in Fig. 2. This is similar to the one used by Xiang *et al.* in their microscope [28, 29]. The outer conductor is extended towards the center conductor with a flat conducting ring. The inner conductor of the transmission line extends beyond the ring through its aperture using a thin wire. The diameter of such wire at its end will determine the probe's spatial resolution. As long as the wavelength in air of the microwaves is much smaller than the ring's diameter and of the distance between the tip and the ring, we may use the quasistatic limit.

The field lines leave the inner conductor's tip towards the ring and outer conductor. In the presence of a sample, some field lines enter the sample just below the tip and exit below

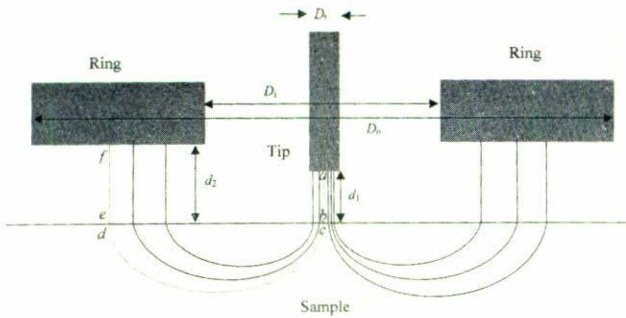

FIGURE 3. Schematic illustration of the electric field lines at the tip-sample region.

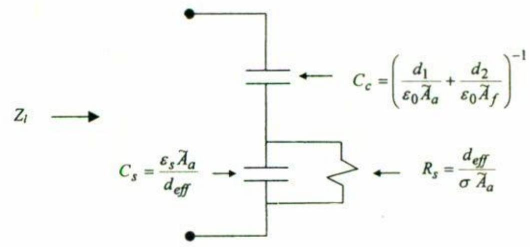

FIGURE 4. Equivalent circuit for the sample.

the ring ending on it. Few of these lines are illustrated schematically in Fig. 3. Let us assume the tip and ring as perfect conductors. Consider one of the mentioned field lines such as the dashed field line in Fig. 3. At any instant of time, the voltage difference between the tip and ring is given by minus the integral of the electric field from point a to f. If d_1 and d_2 in Fig. 3 are small compared with the diameter of the tip and ring respectively, the electric field may be approximated as constant within the gaps. (Thus, $E_a = E_b$ and $E_c = E_f$). Much in the same way as in a parallel capacitor when ignoring fringing fields. The field along the line joining points c to d in the figure will be dependent on the sample's electrical properties and will vary along the length on the line. It will be largest at point c and smallest at point d. We may write the corresponding integral as an effective length times the field at point c: $E_c d_{\text{eff}}$. Thus, the voltage difference at the tip is written as

$$V_l = E_a d_1 + E_c d_{\text{eff}} + E_f d_2. \tag{10}$$

The current density at point c is $\vec{J} = \sigma E_c$, where σ is the conductivity of the sample. The total current may be written as $I = \sigma E_c \tilde{A}_c$, where $\tilde{A}_c$ is an effective area at point c, which commonly will be close to the actual area of the cross section of the tip. On the other hand, the current density may be expressed in terms of the current flow from the interface: $\vec{J} = \sigma E_c = -\delta\rho/\delta t = -j\omega\rho_c$, from where we get $\rho_c = \sigma E_c / j\omega$ (j is the imaginary unit). Applying Gauss' law on the interface between point b and c in the figure, we get $\varepsilon_s E_c - \varepsilon_0 E_b = \sigma E_c / j\omega$. Thus, $E_c = \varepsilon_0 E_b / (\varepsilon_s + \sigma / j\omega)$. The field's amplitude within the gaps may be written in terms of the effective are of the ring ($\tilde{A}_f$) and tip ($\tilde{A}_a$), and the average surface charge on them: $E_a = E_b = \rho_a / \varepsilon_0$ and $E_f = E_e = \rho_f / \varepsilon_0$. The total current I must be expressed in terms of an effective area, as $I = j\omega\rho_a \tilde{A}_a = j\omega\varepsilon_0 \tilde{A}_a E_a$, or as $I = j\omega\varepsilon_0 \tilde{A}_f E_f$. Using both equations yields $E_f = E_e = E_a \tilde{A}_a / \tilde{A}_f$. Hence, the voltage is

$$V_l \cong E_a \left(d_1 + \frac{\tilde{A}_a}{\tilde{A}_f} d_2 + \frac{\varepsilon_0}{\varepsilon_s + \sigma/(j\omega)} d_{\text{eff}} \right). \tag{11}$$

The load impedance Z_l may be calculated as $Z_l = V_l / I$. Using $I = j\omega \tilde{A}_a E_a / \varepsilon_0$ we get from (11),

$$Z_l = \frac{1}{j\omega C_c} + \frac{1}{j\omega C_s + 1/R_s}, \tag{12}$$

where the coupling capacitance is $C_c = (C_1^{-1} + C_2^{-1})^{-1}$, where $C_1 = \varepsilon_0 \tilde{A}_a / d_1$, and $C_2 = \varepsilon_0 \tilde{A}_a / d_2$, the sample capacitance is $C_s = \varepsilon_s \tilde{A}_a / d_{\text{eff}}$, and the sample's resistance is $R_s = d_{\text{eff}} / \sigma \tilde{A}_a$. The equivalent circuit is shown in Fig. 4. If the sample is a nonconductive lossy dielectric, *i.e.*, the dielectric constant is complex, $\varepsilon_s = \varepsilon_s' - j\varepsilon_s''$, σ is replaced (or augmented) by $\omega\varepsilon_s''$, *i.e.*, $R_s = d_{\text{eff}} \varepsilon_s'' / \omega\varepsilon_s' \tilde{A}_a$. In the case of a good conductor we may need to include an inductive element in series with the sample's resistance due to the time varying magnetic field induced by the currents on the sample. For simplicity we will not consider this term (see, *e.g.* Ref. 36).

Using (12) in $g(\omega) = -2Z_0/Z_l$ and defining the sample conductance $g_s = 1/R_s$, we obtain

$$g_r(\omega) = 2Z_0 \frac{\omega^2 C_c^2 g_s}{g_s^2 + \omega^2 (C_c + C_s)^2},$$

and

$$g_i(\omega) = -2Z_0 \omega C_c \alpha$$

where

$$\alpha = \frac{g_s^2 + \omega^2 C_s (C_c + C_s)}{g_s^2 + \omega^2 (C_c + C_s)^2} \tag{13}$$

To a first approximation we may replace α by $\alpha_0 \equiv \alpha$ $(\omega = \omega_0)$ in (12). Thus $(dg_i/d\omega)|_{\omega_0} = -2Z_0 C_c \alpha_0$. Using this result in (8), we obtain to a first approximation,

$$\omega_0' = \omega_0 \left(1 - \frac{1}{2} \frac{C_c}{C_0} \alpha_0 \right), \tag{14}$$

where C_0 is the capacitance of the resonator, $C_0 = \frac{1}{2} C l$, and

$$\alpha_0 = \frac{g_s^2 + \omega_0^2 C_s (C_c + C_s)}{g_s^2 + \omega_0^2 (C_c + C_s)^2}, \tag{15}$$

with $g_s = 1/R_s$.

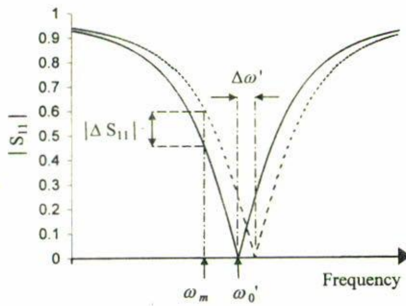

FIGURE 5. Illustration of the resonance curve of $|S_{11}|$, and an induced shift due to the sample interaction. ω_m is the radial frequency where the slope of the resonance curve is largest.

3.3. Sensitivity of the probe

The parameter to measure is the magnitude of the reflection coefficient of the resonator given in (1). Using (15) we have

$$S_{11} = \frac{(R_0' - Z_{0f}) + 2jQ'R_0'\Delta\omega'/\omega_0'}{(R_0' + Z_{0f}) + 2jQ'R_0'\Delta\omega'/\omega_0'} \tag{16}$$

Adjusting the impedance of the feed line so that $Z_{0f} \cong R_0'$ is satisfied close to the resonance frequency, we have

$$|S_{11}| \cong \frac{Q'|\Delta\omega'|/\omega_0'}{(1 + Q'^2\Delta\omega'^2/\omega_0'^2)^{1/2}}. \tag{17}$$

If the resonance frequency ω_0' changes by a small amount $d\omega_0'$ due to a change of the sample coupling, the resonance dip illustrated in Fig. 5 shifts as a whole. If the frequency at which we are measuring $|S_{11}|$ is held fixed at f_x, a small change in the reflection coefficient is registered, $d|S_{11}|$, which is proportional to the derivative of $|S_{11}|$ with respect to frequency. The sensitivity at the frequency ω_m not too far from ω_0' is obtained as

$$\frac{\partial|S_{11}|}{\partial\omega}\bigg|_{\omega_m} \approx s\frac{Q'}{\omega_0'}, \tag{18}$$

where the sign function s is $+1$ or -1 if $\omega > \omega_0$ or $\omega < \omega_0$ respectively. We may then write the change in the resonator's reflection coefficient in terms of a the change of any of the parameters involved in the coupling at the end of the resonator. Hence,

$$\Delta|S_{11}| = \frac{\partial|S_{11}|}{\partial\omega}\bigg|_{\omega_m}\frac{\partial\omega_0'}{\partial t}\Delta t, \tag{19}$$

where t may be d_1, σ, ε_s, etc.. The partial derivative $\partial\omega_0'/\partial t$ may be calculated from (14) and (15).

3.4. Resolution on material properties

The resolution is quantified by the minimum detectable signal (MDS). This is defined as the change in the parameter being imaged which causes a change in the magnitude of the output voltage $|\Delta V_o|$ equal to the rms voltage noise $V_{\rm rms}$. The output signal V_o is given by $V_o = V_i|S_{11}|$ where V_i is the incident voltage wave to the resonator. The output voltage noise is primarily due to circulator noise, detector noise, and amplifier noise. The MDS is calculated from

$$\Delta|V_0| = V_i|S_{11}| = V_i\frac{\partial|S_{11}|}{\partial t}\Delta t = V_{\rm rms},$$

and we get

$$\text{MDS} = |\Delta t|_{\min} = \frac{V_{\rm rms}}{V_i\left|\frac{\partial|S_{11}|}{\partial t}\right|}, \tag{20}$$

where t is the parameter being imaged. The partial derivative $\partial|S_{11}|/\partial t$ is calculated from (19), (18), and (14). We obtain,

$$\text{MDS} = \frac{2C_0V_{\rm rms}}{V_iQ\beta} \tag{21}$$

where $\beta = |C_c\partial\alpha_0/\partial t + \alpha_0\partial C_c/\partial t|$ and we used $\omega_0'/\omega_0 \cong 1$, and $Q \cong Q'$.

To illustrate a few examples let us first consider a perfect dielectric. In this case $g_s = 0$, and thus from (15) we get $\alpha_0 = C_c/(C_c + C_s)$. For a dielectric the effective penetration length is $d_{\rm eff} \approx D_t$ (see Sect. 6 below), thus we commonly have $d_1 \ll d_{\rm eff}$, and for a not too large a dielectric constant ε_s, this results in $C_c \gg C_s$. Let us calculate $|\Delta\varepsilon_s|_{\min}$ and $|\Delta d_1|_{\min}$. The first MDS indicates the ability of the probe to discern between different materials, and the second one indicates the ability to measure height variations of the surface (vertical spatial-resolution). Calculating β from $\alpha_0 = C_c/(C_c + C_s)$ by using $C_s = \varepsilon_s\tilde{A}_a/d_{\rm eff} \approx \varepsilon_s\tilde{A}_a/D_t$ and $C_c = \varepsilon_0\tilde{A}_a/d_1$, we get

$$|\Delta\varepsilon_s|_{\min} = \frac{2C_0V_{\rm rms}\varepsilon_s}{QV_iC_s}, \tag{22}$$

and

$$|\Delta d_1|_{\min} = \left[\frac{2C_0V_{\rm rms}C_c^2}{QV_iC_s^2}\right]\left[\frac{d_1}{C_s}\right]. \tag{23}$$

Let us consider a numerical example. Typical values for a EMP based on a microstrip resonator are $Q = 1000$, $V_i = 10$ V, $V_{\rm rms} = 20$ mV, $C_0 = 3 \times 10^{-12}$ F [38, 41]. Let us assume a tip of circular cross section with a diameter of $D_t = 100\,\mu$m at a distance $d_1 = 1\mu$m from the sample's surface, and an operating frequency of 1 GHz, $\omega_0 = 2\pi \times 10^9$. Thus the effective area is $\tilde{A}_a = 7.85 \times 10^{-9}$ m^2; and by assuming $C_1 \ll C_2$, we get $C_c \approx C_1 = 7 \times 10^{-14}$ F. From (22) we get the MDS for the dielectric constant in the present example, $|\Delta\varepsilon_s|_{\min}/\varepsilon_0 = 0.017$. From (22) it can be shown that increasing the tip's diameter D_t decreases in the same proportion $|\Delta\varepsilon_s|_{\min}/\varepsilon_0$, thus improving the resolution. From (23) we get $|\Delta d_1|_{\min} = 1.7 \times 10^{-6}(\varepsilon_0/\varepsilon_s)^2$ m. For $\varepsilon_s = 10$, this is already in the nanometer scale. Of course, in any case increasing the resonator's Q, decreasing the resonator's capacitance C_0, or decreasing the ratio $V_{\rm rms}/V_i$ would improve the resolution in a linear relation.

Let us consider the same probe values in an example with a semiconductor. The minimum detectable change in the coupling resistance R_s is found following the above procedure as $|\Delta R_s|_{\min} = [(2C_0V_{\rm rms})\ /(QV_i)][(1 + R_s^2\omega_0^2C_c^2)^2/2R_s\omega_0^2C_c^3]$. Using $R_s = r_s d_{\rm eff}/\tilde{A}_a$, where r_s is the resistivity, we get

$$|\Delta r_s|_{\min} = \left[\frac{2C_0V_{\rm rms}}{QV_i}\right] \times \left\{\frac{[1 + r_s^2\omega_0^2C_c^2(D_t/\tilde{A}_a)^2]^2}{2r_s\omega_0^2C_c^3}\right\}\left(\frac{\tilde{A}_a}{D_t}\right)^2, \quad (24)$$

where we used $d_{\rm eff} \approx D_t \ll \delta$ (see Sect. 6 below). As a numerical example, we obtain from (24) for the present example $\Delta r_s|_{\min}/r_s = 2.7 \times 10^{-2}$, 4.7×10^{-4}, 2.9×10^{-3}, 0.3, and 28, for $r_s = 10^{-2}$, 10^{-1}, 1, 10, and $10^2\ \Omega$m, respectively. Note that $|\Delta r_s|_{\min}$ is a complicated function of ω_0, D_t, d_1, and r_s. Thus, by using (24) one should choose the tip's diameter and distance to maximize resolution for the expected range of resistivity. Since our model does not include an inductive term in the coupling impedance, we can not extend our calculations to good conductors, such as metals. This case is considered in Ref. 41. Following a similar procedure, and assuming a resistivity of $r_s \approx 0.1\ \Omega$m, we obtained $|\Delta d_1|_{\min} = 2 \times 10^{-10}$ m for the present example. This is a quite impressive resolution, comparable to what one can get with optical techniques in practice.

Note that when imaging a perfect dielectric [formulas (22) and (23)], the only dependence on λ is due to the frequency dependence of C_s due to the dispersion characteristics of the dielectric constant ε_s. In the case of a semiconductor, there is some additional dependence on the frequency, according to (24).

4. Differences with other electromagnetic probes

As mentioned above, EMP may be regarded as related to NSOM and to SCM. However, direct relation between NSOM and SCM is not obvious, if any. In this sense, an EMP may be considered as "in between" SCM and NSOM. We discuss in this section the main differences and advantages of EMPs with respect to SCM and NSOM.

At microwave (MW) frequencies very good conductors exist, while at visible and near infrared frequencies real metals are fairly poor conductors. Hence, at MW frequencies low-loss transmission lines are a practical realization. Transmission lines propagate TEM waves which have no cut-off frequency. The electromagnetic field is confined within metallic conductors and allows to concentrate the power flux across an area with linear dimensions much smaller than the wavelength.

Attempts to implement and use transmission lines at optical frequencies for NSOM have not been successful [13]. In the optical regime, dielectric waveguides are used. Dielectric waveguides, with few exceptions, propagate TE and TM modes only, all of which have a cutoff frequency. For a thin waveguide with dimensions smaller than a wavelength these modes are not present. In step-index waveguides with circular cross section, the fundamental hybrid mode EM_{11}, is one of the exceptions, and has no cutoff [46]. In NSOM the tip may be formed by tapering the end of a optical fiber. At the tip, the core has disappeared and the cladding of the fiber becomes the core. Forming a step index fiber: cladding-air. At the tip the only guided mode is the fundamental mode. However, the lateral profile of the energy density in the optical field of the EM_{11} mode remains in the order of the wavelength, even though, the dimensions of the core may be small compared to the wavelength. Thus, power cannot be confined to dimensions much smaller than the wavelength and resolution is not much smaller than the wavelength. On the other hand coupling efficiencies to the tip is in the order of 10^{-6} [13]. Other possibility is to cover the tapered region of the optical guide with a metal layer. The fundamental mode becomes then the TE_{11}. This mode, though, cutoffs at a normalized (with respect to λ) core radius of 0.2. It decays exponentially for smaller core radius. For common taper angles the power loss to the apex would render the tip useless. An optimal metal-coated tip would taper gradually to cutoff, where it would end abruptly. An aperture in the metal coating on the blunt end of this tip would then provide further confinement of the light and enhance spatial-resolution. The aperture diameter should be at most in the order of the skin depth of the light in the metal. Otherwise the aperture would work as an over-damped waveguide resulting in further losses. The resulting limit on resolution for these probes is roughly 10 nm for green light for the best available metal (aluminum) [13]. Thus, the resolution is limited due to the skin depth of light into the metal. In either case, the power losses on coupling light into a small area with linear dimensions small compared to the wavelength are very strong. Requiring to work in the lower limit of the current photon-detection technology. This makes NSOM expensive and requiring special care.

The above problems in NSOM are absent in EMP, being this an important difference of EMP with regard to sub-wavelength imaging. As discussed in Sect. 3, the limit to the spatial resolution in EMP comes from the unwanted coupling that may occur between the tip and the external conductor of the transmission line, and of the resistance of the tip that comes with reducing its diameter. A 100 nm resolution has been achieved, but theory predicts that smaller resolutions should be possible in many cases [40]. Apparently EMP will achieve similar spatial resolutions than aperture-based NSOM, although the wavelength is typically five orders of magnitude larger.

SCM using a UHF (ultrahigh frequency) resonant circuit [17–19] is also closely related to EMP, in fact SCM may be considered as a precursor of EMP. The coupling capacitance between the tip and sample plays a central role in either technique, and both may use a resonant structure to measure

the coupling between sample and tip. The main difference between the two probes is that capacitance microscopy uses a conducting substrate, which is generally grounded to the casing of the resonant circuit. EMP, on the other hand, can be used to image insulators (with no conducting substrate). In an EMP the ground is the external conductor in the transmission line, which may be tapered or extended by a shielding metallic ring. EMP are also sensitive to the surface resistance and to a effective inductance [41]. In EMP the signal is less sensitive to the background than in SCM, since the induced currents are confined below the tip. In SCM spatial resolutions in the order of 25 nm have been reported [17], while in EMP the record resolution to date is 100 nm. In general we may expect that comparable resolutions should be achieved with both techniques. As indicated, resolutions in the few nm range are expected for EMP [40].

5. Applications of EMP

The EMP signal depends on the electric permitivity ε, magnetic permeability μ, and conductivity σ, of the sample as well as on the topography of the surface. ε, μ, and σ, are in general complex quantities and depend on different physical and chemical parameters: Temperature, chemical composition, moisture, stress, strain, density, etc. Thus, all the later parameters may be imaged with an EMP for different applications.

Many important physical effects have temporal spectrums in the microwave regime; *e.g.* rotation of small molecules, bending modes of macromolecules, etc. Liquid water, being a very important component of biological systems, absorbs strongly in the microwave regime. On the other hand, the conductivity at MW frequencies is commonly close to the DC conductivity, making the EMP a potentially very useful non-destructive tool for the electronic industry.

EMP may be recognized as a non-contact and non-destructive tool for the imaging of insulators, semiconductors, and metals. EMP compliments optical and electronic microscopes in the range of 0.01 μm to 1 cm. One attractive feature of EMP for applications is that a minimum of sample preparation is generally needed. The distance between probe and tip may vary from a small fraction of a micrometer to a few hundreds of micrometers, or more. The spatial resolution being strongly dependant on the tip-sample separation (once this is larger than the tip's diameter). In the case of some insulating samples with smooth surfaces, physical contact between the tip and sample can be used to enhance resolution.

Many applications do not require sub-micron resolutions, but a large imaged area. Lower spatial resolution permits to scan the EMP probe further away from the sample's surface. In these cases EMP may offer new unique possibilities, such as subsurface imaging while allowing large surface roughness, imaging of sticky surfaces, and high sensitivity to material parameters. With relatively large tip-sample separations it is also possible to image very hot surfaces. Subsurface features in metals can be imaged due to the larger penetration lengths of microwaves compared to infrared and optical waves. Scan rates of 0.1 mm/S have been achieved with the possibility of increasing it by a factor of 10 [32]. Such scan rates are relatively very fast (*e.g.* compared with STM and AFM), and yield EMP suitable for on-line and quality control applications.

As a non-destructive tool, EMP has the advantage over ultrasonic testing of insulators in that MW have relatively high transmission coefficients across solid-air boundaries. Also, ultrasound absorption coefficients are much higher than MW in dielectrics.

On the limitations of EMP we may point out the fact that the signal depends on the material parameters, tip-sample distance, and topography, making it necessary in some cases to compliment an EMP with a independent sensor to deal with the tip-sample separation. An optical fiber sensor has been used for this purpose in Refs. 35 and 37. Image interpretation is then not always trivial and may require detailed modeling of the EMP signal and some assumptions on the sample. Of course, similar limitations apply to other local probe microscopes as well. In the following subsections, we summarize recent work on applications of EMP.

5.1. Dielectrics

A two dimensional map of the dielectric constant of a sample consisting of three dielectric layers, 1mm wide each, and with dielectric constants of 11.8, 5.5, and 3.6 was given in [35]. The minimum detectable change in the dielectric constant was determined to be 1.7%. Images of a 2×3 mm^2 region of a carbon composite were obtained in Ref. 34. Delaminated regions are clear in the image when compared to the image of an intact sample. Imaging of the dielectric constant profile with very high resolution (≈ 100 nm) of a thin dielectric film grown in saphire substrate by dip coating was done in Ref. 29. For such high resolution the authors allowed soft contact (force $< 20\,\mu$N) between tip and sample.

5.2. Semiconductors

Doped silicon wafers have been used to calibrate a EMP signal as a function of resistivity [35]. Also variation in resistivity induced on a doped simiconductor upon shining light onto it has been measured with an EMP [34]. A resistivity map over a 4″1.5 μm 3C-SiC on Si wafer was obtained using an EMP (non-contact measurement) in Ref. 34. Since the microwave probe response is quite fast ($< 0.1\,\mu$s), the response of the semiconductor to an external stimulus, such as an optical pulse or depleting high-power electromagnetic pulse, can be monitored. In the later work, the response of a B-doped silicon sample to pulses of light generated by a GaAs laser diode was monitored through time using an EMP. Transient measurements can be performed at different temperatures, and since the microwave probe measurement is non-contact, only the sample has to be heated or cooled. Activation en-

ergies and various parameters of deep levels, such as their capture/emission cross sections, and densities can be determined. In the later experiment the carrier recombination lifetime was calculated from the EMP signal. Also the response of a photoresistor to an optical pulse and then to heating by a 40 mA pulse of current was monitored through time with an EMP in Ref. 36. These experiments showed clearly the feasibility of using an EMP to monitor various processess that may take place inside a semiconducting materials.

5.3. Metals

A MW image of a printed circuit board using an EMP was reported in Ref. 27. A previously drilled hole covered with solder was clearly visible in the image; demonstrating the capability of subsurface defect detection capabilities of EMP. In Ref. 33 it is shown that an EMP can be operated in the transmission mode to detect buried metallic lines in poorly conducting materials. In Ref. 34 an EMP is used to image a 2 mm diameter hole on a 6 mm thick copper plate. It was found that on doing a line scan across the hole, burrs at the edges can be detected and characterized to some degree. In the same work it was shown that an EMP can detect residual stress in metals based on the capability of detecting subsurface conductivity differences. A scanning image of two Nb strips, 1000 Å thick, 10 μm wide, and 20 μm apart was taken in Ref. 28. The image of an array of squared Cu films through glass was also taken in the later work. The dimensions were 300 μm$\times$300 μm and 1000 Å thick in one case, and 500 μm $\times$500 μm and 2000 Å thick in other case. The tip separation was 200 μm.

The use of an EMP to image active microwave circuits was suggested and demonstrated in Ref. 30. The EMP is converted to a receiving mode and acts as a local microwave pickup. The image in a receiver mode of an excited microstrip at 8.5 GHz was taken. The image shows clear microwave standing wave excitation on the microstrip. Steinhauer *et al.* [31] measured the resonance frequency of their EMP as a function of surface resistance in the range 58 $\Omega/\square$ to 42 $K\Omega/\square$. The sample consisted of a variable-thickness thin-film of oxidized aluminum on glass subtrate.

5.4. Biological and medical applications

The moisture-content map of a small region of a plant leaf was obtained using a EMP in Ref. 34. Some basic features of the leaf, seen on an optical image, could be seen also on the MW image. In the same work, higher moisture content regions in balsa wood was also imaged clearly. Polished specimens of control and trabecular bone of a human femur were imaged using an EMP [32]. For comparison the samples were imaged using scanning acoustic microscopy (SAM). The imaging was done (in both cases) maintaining the samples in a fluid environment. (demonstrating the feasibility of imaging through a liquid with an EMP.) Results show the possibility of imaging at the same time the elastic and electrical properties of skeletal tissue at the micrometer level. In the same work the image of the cross section of a human tooth was obtained. The authors speculated on the possibility of detecting incipient caries without obvious clinical nor radiographic manifestation. Of course, EMP may be applied to other biological tissues, such as skin, cartilage, etc. In general, water and mineral content (such as Na^+ and K^+), being important biological constituents can affect the dielectric constant and conductivity.

5.5. Temperature variations

Variations in temperature of a resistive strip can be monitored as a function of time in a point measurement using an EMP. The mechanism is through variations in the local conductivity due to a change in temperature. Experimentally a resolution of 0.08°C was determined for the sample used in Ref. 36. In the same work, transient heating of a photoresistor by a 40 mA pulse of current was monitored using an EMP. The results of this work indicate the capability of an EMP to do spatial and temporal thermography.

5.6. Novel physical and chemical sensors

In Ref. 37 an EMP was used to monitor the resistivity of a Pd film on a cantilever as a function of Hydrogen concentration. The resistivity changed by 13.5% at 3.0% concentration of H_2 and it resulted in a change of 18% of the EMP signal. Hydrogen concentration in the range 0.01% to 4% could be detected. As the Pd film absorbs H_2 it expands and the cantilever beam deflects downwards. Such deflection could also be detected by the EMP. The EMP with an appropriate frequency can also be used to resonantly detect physiabsorbed molecules at the surface of an appropriate material as well. The performance of an EMP as a displacement sensor (displacement of a cantilever) was addressed in detail recently [38]. Displacement sensing in the range 0.01 μm to 5 cm is possible.

Point sensors are of interest because it could be possible to integrate a large number of them into a reasonably sized sensor panel. Selectivity and stability problems may be solved using signal processing of all sensor outputs. This, by the way is the solution nature has chosen in biological creatures. For point sensors using EMP to be practical it would be needed to integrate the whole EMP into a single chip. EMP have been fabricated on high-resistivity silicon using standard "lift-off" photolitography processes [39]. The Q factors of the fabricated resonators was very high ($\approx$ 13 000). This may enable integration of arrays of EMP and silicon cantilevers for point chemical or physical sensors.

6. On the transverse spatial resolution

The transverse resolution of the probe will clearly depend on the tip's diameter D_t. Assuming that the distance to the sample d is much smaller than D_t, the field lines will be very in-

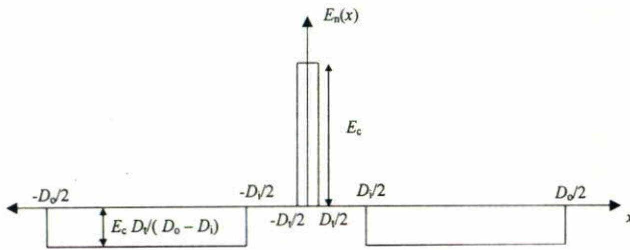

FIGURE 6. Assumed distribution (to a first approximation) of the normal component of the electric field at the sample's surface.

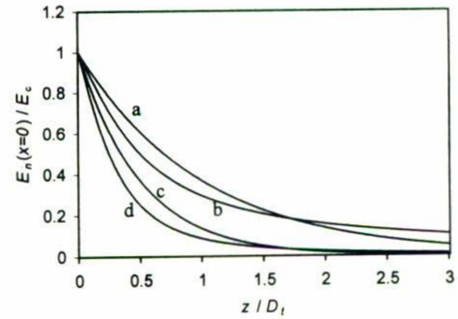

FIGURE 7. Decay of the normal component of the electric field, E_n (curve b), and its square, $|E_n|^2$ (curve d), below the center of the tip ($x = 0$) as a function of z inside the sample. The curves $\exp(-z/D_t)$ and $\exp(-2z/Dt)$ are shown for comparison (curves a and c respectively).of the tip ($x = 0$) as a function of z inside the sample.

tense just below the tip and its magnitude will decrease rapidly with distance. The effective area $\tilde{A}_a$ is close to the transverse area of the tip if $d_1 \ll D_t$. Thus, the spatial transverse resolution of the probe will be in the order of D_t. Recall that we are assuming a flat end of the tip. Thus, the spatial resolution will be increased by tapering the tip to achieve a smaller D_t. Recently Gao *et al.* [40] considered the imaging of dielectrics with the tip as a conducting sphere and showed that the spatial resolution can be one or even two orders of magnitude less than the radius of the tip's sphere.

Other concern is the penetration depth of the electromagnetic field within the sample. On the one hand it is important if subsurface features are of interest. This, by the way, may be a very attractive feature of EMP. But on the other hand, the spatial transverse-resolution should be related in some manner to the penetration depth. In general we may expect that the spatial transverse resolution cannot be appreciably smaller than the penetration depth of the electromagnetic field in the sample. Continuing with the same tip model, the penetration depth is related to d_{eff}, the effective length of the integration path inside the sample in (10). If the tip diameter D_t (see Fig. 3) is much smaller than the inner radius of the conducting ring D_i, the field lines will be of largest magnitude just below the tip. As we move along the field line towards the ring, the field magnitude will decrease rapidly (consider the dashed field line in Fig. 3). Thus, the main contribution to the integral comes from the first portion of the field line.

In the case of a good conductor (displacement current can be neglected), the field magnitude decays exponentially inside the sample. The decay constant being the "skin-depth", $\delta = \sqrt{2/\omega\mu\sigma}$, where μ is the permeability of the sample [44]. In this case, d_{eff} will be in the same order of magnitude as δ. In the case of dielectrics, d_{eff} will be in the order of the decay distance of the evanescent fields. To get an idea of the penetration length in this case, we may consider the plane wave expansion within the sample of the normal component of the electric field E_n. Simplifying things, to a first approximation the normal component of the field just below the interface of the sample is assumed distributed as illustrated in Fig. 6. For ease of illustration, let us consider a two dimensional situation, *i.e.*, $E_n = E_n(x)$ in what follows. Recall that $E_n(x)$ is proportional to the surface polarization charge on the dielectric. Thus the integral of $E_n(x)$ along x is zero if the dielectric is to remain electrically neutral as a whole. Then, by Fourier transforming $E_n(x)$ depicted in Fig. 6, and writing the inverse Fourier transform, with $\exp[j\sqrt{\varepsilon_s k_0^2 - k_x^2}z]$ multiplying the Kernel, one obtains an expression for the field $E_n(x,z)$, below the sample's surface. Whenever $k_x^2 > \varepsilon_s k_0^2$ the square root is imaginary and the contribution to the integral is an evanescent wave (exponentially decaying). The field just below the center of the tip ($x = 0$) as a function of z (within the sample) is found from integrating the inverse Fourier transform with the Kernel evaluated at $x = 0$. Neglecting the term $\varepsilon_s^2 k_0^2$ inside the square root (electrostatic limit) the integral to be done is found in published tables of integrals. We get

$$E_n(x=0,z) = \frac{2E_c}{\pi}\left\{\tan^{-1}\left(\frac{D_t}{2z}\right) - \frac{D_t}{D_0 - D_i}\left[\tan^{-1}\left(\frac{D_0}{2z}\right) - \tan^{-1}\left(\frac{D_i}{2z}\right)\right]\right\}. \quad (25)$$

In Fig. 7 we plot E_n/E_c from (25) as a function of z/D_t for $D_o = 200\,D_t$ and $D_i = 50\,D_t$ (curve b). The curve is practically insensitive to the values of D_o and D_i once D_o is larger than about 50 times D_t (and $D_t < D_i < D_o$). Thus, the curve is basically the same for other values of D_i and larger values of D_o. The curve for $\exp(-z/D_t)$ is shown for comparison (curve a). The square of the corresponding curves is also shown (lower curves, d and c respectively). From the figure we see that the field E_n has decayed to 0.3 times its value at the surface of the sample at $z = D_t$. The field energy density (proportional to E_n^2) has decayed 90% at $z = D_t$. Thus, the simple model above predicts a penetration length in the order of the tip's diameter. In general, the penetration length will be the smaller between the skin depth δ and the evanescent field penetration ξ obtained from (25). The possibility of imaging subsurface structures will be determined by the penetration length. It is clear that there is no dependence of the transverse spatial resolution on the wavelength when the tip-sample distance is smaller than the tip's diameter, since the field pattern is practically of electrostatic nature.

There will be limitations to reducing D_t for different reasons. On the one hand, reducing the diameter of the tip increase the resistivity of the tip itself. On the other hand, reducing the aperture's diameter on the shielding ring (D_i), may result in unwanted coupling between the inner and outer conductors forming the transmission line. Both effects would tend to reduce the Q of the resonator and thus the sensitivity and resolution. Of course, the tip geometry and the tip-sample interaction should be addressed in more detail and more laborious models should be studied in the future to answer quantitatively the fundamental questions on the EMP and the quantitative interpretation of the imaging.

6.1. Enhancing resolution

6.1.1. Syncronous detection

The signal in a EMP is affected by low frecuency noises which tend to be larger. An interesting possibility for a more sophisticated detection scheme is to vibrate the sample (or the tip) at a fixed frequency. The tip-sample distance being then an harmonic function of time. The resulting AC signal has an amplitude proportional to the first derivative of the coupling capacitance with respect to the tip-sample distance. This first derivative is a stronger function of distance than the capacitance. On the other hand the signal's amplitude can be measured synchronously using a lock-in amplifier reducing considerably the effect of random electrical noise, which is the dominant noise in EMP. This detection scheme has already been used showing an improvement in resolution [35].

6.1.2. Deconvolution algorithm

A simple deconvolution method was developed in Ref. 42 and used to sharpen the images taken with an EMP. The deconvolution of EMP images improved the spatial resolution by at least a factor of 2 in cases in which the inherent spatial resolution was very high ($0.4\,\mu$m) and by a factor of 4 when the resolution was low ($40\,\mu$m). The method is based on measuring the spatial impulse response (or point spread function) of the probe. Assuming that, to a good approximation, the EMP image is the convolution of the experimental spatial-impulse response, this function is used to deconvolve the image. These results give motivation to improve the current models of the tip-sample interaction and tip design.

6.1.3. Analytical tools

Numerical schemes (such as finite difference methods) are useful tools in modeling the tip sample coupling. However, when dealing with two-dimensional problems, numerical calculations require excessive computer memory. Additionally, numerical schemes do not provide much physical insight into the problem. Analytical approximate results can be very useful when dealing with real two-dimensional structures and can provide better accuracy with much less effort. Furthermore, analytical results may provide, in some cases, inverse algorithms for image interpretation and spatial resolution enhancement.

When accurate to model the tip as a conducting sphere and the sample's surface as flat, simple analytical results can be obtained [40]. However, for very-high resolution, in which $d_1 \ll D_t$, it may be more appropriate to model the sensing region of the tip as a flat electrode with some protrusion actually functioning as the tip and a rough surface of the sample. In this case, few analytical tools have been developed. Recently the problem of a capacitor with a rough electrode has been addressed. Analytical results that may allow to calculate accurately the capacitance have been studied based on a perturbative solution to the boundary integral equations [43], and extensions have been sought using a simple approach suggested by the Padé-approximation method [44]. Until now, only one electrode has been considered rough. It is necessary to extend the work to the case of two rough electrodes with a clear protrusion working as the tip. Also, it will be necessary to extend the work to deal with one rough electrode, a rough dielectric interface and a flat electrode. These extensions are in principle possible and should be studied in the future.

7. Summary and final comments

We presented an overview of the development and present state of development of the Evanescent Microwave Probes and their use in microscopic characterization of materials. The EMP is a novel non-destructive non-contact tool for the characterization or sensing of insulators, semiconductors and metals. EMP can obtain a two-dimensional image of the microwave properties of materials with very high-resolution. Images of the topography and subsurface features can be obtained as well. The EMP compliment other microscopy techniques in the range of sub-micron to millimeter resolution.

Among the principal attractive features of these probes is their relative simplicity, the lack of time consuming sample preparation, wide range of spatial-resolution (submicron to millimeter resolutions), fast scan rates, and high sensitivity to electrical parameters of the sample. Among the most attractive capabilities of these probes are: Non-contact surface resistance measurement and imaging of cold and hot surfaces, novel biological and medical applications, and sub-surface imaging of defects in metals.

Theoretical modeling of the tip-sample interaction for the quantitative interpretation of images and for improving the tip designs for each application should be a line of further research. An evaluation of the different signal processing schemes proposed to date should be also of interest, as well as proposing new techniques. No fundamental resolution limit has been formulated to date, and more analysis in this respect is needed. Spatial resolution in the few nanometer range are expected to be possible in many cases.

EMP may also be regarded as the core for a new class of sensors. Integration of microwave resonators with electronics

in a single chip is already under investigation and may open a wide range of possibilities in creating new sensors and panels of sensors for chemical and biological applications. Many new applications of EMP are still awaiting to be explored. As with most near field probes, new technical and theoretical issues will arise with new applications.

---

1. G. Binning and H. Rohrer, *Helv. Phys. Acta.* **55** (1982) 726.
2. G. Binning, H. Rohrer, Ch. Gerber, and E. Weibel, *Appl. Phys. Lett.* **40** (1982) 178; *Phys. Rev. Lett.* **50** (1983) 120.
3. G. Binning, C.F. Quate, and Ch. Gerber, *Phys. Rev. Lett.* **56** (1986) 930.
4. S. Alexander *et al.*, *J. Appl. Phys.* **65** (1989) 164.
5. Y. Martin and H.K. Wickramasinghe, *Appl. Phys. Lett.* **50** (1987) 1455.
6. C.C. Williams and H.K. Wickramasinghe, *Proc. SPIE* **897** (1988) 129.
7. P.K. Hansma *et al.*, *Science* **243** (1989) 641.
8. D.W. Pohl, W. Denk, and M. Lanz, *Appl Phys. Lett.* **44** (1984) 651.
9. J.R. Matey and J. Blanc, *J. Appl. Phys.* **47** (1985) 1437.
10. U. During, D.W. Pohl, and F. Rohner, *J. Appl. Phys.* **59** (1986) 3318.
11. A. Lewis, M. Isaacson, A. Murray, and A. Harootunian, *Biophys. J.* **41** (1983) 405.
12. E. Betzig *et al.*, *Biophys. J.* **49** (1986) 269.
13. M.A. Paesler and P.J. Moyer, *Near-field optics: Theory, instrumentation, and applications*, (John Wiley & Sons, Inc., New York, 1996).
14. D. Pohl, European patent application no. 0112401, Dec. 27 1982; US patent 4 604 520, Dec. 20 1983.
15. (All articles in No.1-4) *Ultramicroscopy* **71** (1998).
16. C.D. Bugg and P.J. King, *J. Phys. E* **21** (1988) 147.
17. C.C. Williams, W.P. Hough, and S.A. Rishton, *Appl. Phys. Lett.* **55** (1989) 203.
18. R.C. Barret and C.F. Quate, *J. Appl. Phys.* **70** (1991) 2725.
19. G. Neubauer *et al.*, *J. Vac. Sci. Technol. B* **14** (1996) 426.
20. E.H. Synge, *Philos Mag.* **6** (1928) 356.
21. H.A. Bethe, *Phys. Rev.* **66** (1944) 163.
22. A.V. Baez, *J. Opt. Soc. Am.* **46** (1956) 901.
23. R.F. Soohoo, *J. Appl. Phys.* **33** (1982) 1276.
24. E.A. Ash and G. Nicholls, *Nature* **237** (1972) 510.
25. C. Julian Chen, *Introduction to scanning tunneling microscopy*, (Oxford University Press, New York, 1993).
26. R.J. Gutmann, J.M. Borrego, P.C hakrabarti, and Wang Ming-Shan, *IEEE MTT-S Digest*, (1987) 281.
27. M. Tabib-Azar, N.S. Shoemaker, and S. Harris, *Meas. Sci. Technol.* **4** (1993) 583.
28. T. Wei, X.D. Xiang, W.G. Wallace-Freedman, and P.G. Schultz, *Appl. Phys. Lett.* **68** (1996) 3506.
29. Chen Gao *et al.*, *Appl. Phys. Lett.* **71** (1997) 1872.
30. C.P. Vlahacos *et al.*, *Appl. Phys. Lett.* **69** (1996) 3272.
31. D.E. Steinhauer *et al.*, *Appl. Phys. Lett.* **71** (1997) 1736.
32. M. Tabib-Azar, S. Bumrerraj, J.L. Katz, and S.R. LeClair, (1999) (submitted).
33. M. Tabib-Azar, R. Ciocan, G. Ponchak, and S.R. LeClair, (1999) (submitted).
34. M. Tabib-Azar, P.S. Pathak, G. Ponchak, and S.R. LeClair, *Rev. Sci. Instrum.* **70** (1999) 2783.
35. M. Tabib-Azar *et al.*, *Rev. Sci. Instrum.* **70** (1999) 1725.
36. M. Tabib-Azar, R. Ciocan, G. Ponchak, and S.R. LeClair, *Rev. Sci. Instrum.* **70** (1999) in press.
37. M. Tabib-Azar, Boonsong Sutapun, G. Ponchak, and S.R. LeClair, (1999) (submitted).
38. M. Tabib-Azar, Deji Akinwande, G. Ponchak, and S.R. LeClair, *Rev. Sci. Instrum.* **70** (1999) (in press).
39. M. Tabib-Azar, D. Akinwande, G. Ponchak, and S.R. LeClair, *Rev. Sci. Instrum.* **70** (1999) (in press).
40. C. Gao and X.D. Xiang, *Rev. Sci. Instrum.* **69** (1998) 3846.
41. M. Tabib-Azar, D.P. Su, S.R. LeClair, and G. Ponchack, (1999) (submitted).
42. M. Tabib-Azar, R. Ciocan, S.H. You, and S.R. LeClair, (1999) (submitted).
43. A. García-Valenzuela, Bruce C. Neil, and D. Kouznetsov, *J. Phys. D. Appl. Phys.* **31** (1998) 240.
44. N.C. Bruce, A. García-Valenzuela, and D. Kouznetsov, *J. Phys. D. Appl. Phys.* (1999) (submitted).
45. R.E. Collin, *Foundations of microwave engineering*, (McGraw-Hill, Singapore, 1966).
46. S. Ramo, J.R. Winnery, and T. Van Duzer, *Fields and Waves in Communication Electronics*, (Wiley, New York, 1994).